

ORIGINAL RESEARCH ARTICLE

Microstructure, mechanical properties, and corrosion performance of additively manufactured CoCrFeMnNi high-entropy alloy before and after heat treatment

Roman Savinov, Jing Shi*

Department of Mechanical and Materials Engineering, College of Engineering and Applied Science,
University of Cincinnati, Cincinnati, OH 45221, USA

Abstract

Equiatomic CoCrFeMnNi, one of the well-known high-entropy alloys, possesses attractive mechanical properties for many potential applications. In this research, the effects of heat treatment on additively manufactured CoCrFeMnNi materials were studied. A pilot experiment was conducted to select two selective laser melting (SLM) conditions of different laser scanning speeds based on the density and porosity of obtained materials. Thereafter, microstructure, tensile properties, impact fracture, microhardness, and corrosion resistance were investigated for the materials obtained under the two selected SLM conditions, with and without heat treatment. It was discovered that while the texture with a strong $\langle 100 \rangle$ alignment was observed in both as-built and heat treated materials, the texture of heat treated materials was stronger. Also, heat treatment drastically improved the ductility of as-built CoCrFeMnNi by 23 – 59% for the selected SLM conditions, while the ultimate tensile strength showed only negligible change. The increase of ductility was believed to result from the release of residual strain and the increase of average grain size after heat treatment. Moreover, heat treatment was able to bring noticeable improvement in energy absorption for the as-built CoCrFeMnNi, reflected by 11 – 16% more energy absorption. Besides, all studied materials showed signs of ductile fracture, but more signs of brittle fracture, such as cleavage facets, were found in the as-built materials as compared with the heat-treated materials. In addition, higher laser scan speed was found to cause moderate reduction in corrosion resistance. Effect of heat treatment was also negative and mild for lower scanning speed case. However, the highest reduction in corrosion resistance was observed after heat treatment of the high laser scanning speed case.

Keywords: CoCrFeMnNi; High-entropy alloy; Additive manufacturing; Selective laser melting; Properties; Microstructure

*Corresponding author:

Jing Shi
(jing.shi@uc.edu)

Citation: Savinov R, Shi J, 2023, Microstructure, mechanical properties, and corrosion performance of additively manufactured CoCrFeMnNi high-entropy alloy before and after heat treatment. *Mater Sci Add Manuf*, 2(1): 42.
<https://doi.org/10.36922/msam.42>

Received: November 9, 2022

Accepted: December 28, 2022

Published Online: February 9, 2023

Copyright: © 2023 Author(s). This is an Open Access article distributed under the terms of the Creative Commons Attribution License, permitting distribution, and reproduction in any medium, provided the original work is properly cited.

Publisher's Note: AccScience Publishing remains neutral with regard to jurisdictional claims in published maps and institutional affiliations.

1. Introduction

Until recently, the main strategy used in material engineering to produce alloys was choosing a principal element and adding several secondary elements to it. Such principal element approach considerably limits the scope of alloy development^[1]. Common

metallurgy knowledge suggests certain correlation between the number elements in a multicomponent system and the number of phases and intermetallic compounds formed in such system. In 2004, Yeh *et al.*^[2] showed that single or double solid solutions can become stabilized when multiple elements are mixed in an appropriate ratio. This can happen because configurational entropy of mixing such elements is high enough to overcome the enthalpy of compound formation^[1]. This new class of materials was named as high-entropy alloys (HEAs). HEAs can be defined with respect to composition or entropy. For composition-based definition, HEAs are usually the alloys containing at least four dominant elements with atomic percentage between 5% and 35%, in which additional minor elements are allowed if their atomic percentage is <5%. For entropy-based definition, entropy of mixing is calculated for alloys^[1]: $S_{mix} = -R \sum_{i=1}^n x_i \ln x_i$, where R is the gas constant and x_i is the molar fraction of the i -th element in the mixture, and the alloys with entropy higher than $1.5R$ are considered HEAs^[4].

A major type of HEAs has been developed based on the parent alloy of CoCrFeNi, which consist of a single face-centered cubic unit cell (FCC) solid solution without segregation^[5]. The addition of more elements to this HEA can reduce the diffusion, which enhances microstructure and mechanical properties such as creep resistance. For instance, CoCrFeMnNi, which also consists of a single-phase FCC, was first studied by Cantor *et al.*^[6], and now it is known as “Cantor alloy.” This alloy is one of the most thoroughly investigated HEAs, and it exhibits some attractive mechanical properties, such as unusual combination of high yield strength, high ultimate tensile strength, high ductility and fracture toughness at cryogenic temperatures^[7]. The damage-tolerance can be attributed to the low stacking fault energies (SFEs) ranging from 18.3 to 27.3 mJ/m²·m⁻² at room temperature^[8]. The Cantor alloy was also shown to exhibit good radiation resistance. Damage-tolerance also rises from high lattice friction stress which results from the apparently random distribution of the solutes. This forms a true solid solution down to atomic scale which leads to high resistance to dislocation motion.

Unfortunately, the applications of HEAs are often plagued by the availability of manufacturing methods. Traditional manufacturing approaches are either expensive or inefficient in dealing with complex shapes, while additive manufacturing (AM) technology is well positioned to overcome such challenge thanks to its nature of layer-wise fabrication and significantly simplified process steps^[8-10]. Compared with other AM techniques, selective laser melting (SLM), featured with high geometrical accuracy and

product surface finish, has become a major AM technique for making complex metal components. Note that SLM belongs to the general powder bed fusion (PBF) group of AM processes according to the ISO/ASTM classification. In SLM, localized laser heating and high laser scanning speed result in extreme short duration of laser-material interaction^[11]. The resultant rapid cyclic heating and cooling process is the root cause for the unique microstructure and mechanical properties of SLMed materials. SLM process may also produce favorable properties for HEAs. For instance, it was discovered that CoCrFeNi HEA obtained from SLM possess much higher yield strength compared with that produced by arc melting^[12]. Li *et al.*^[13] investigated SLM-produced CoCrFeMnNi and observed that elongated columnar grains grew epitaxially with a <001> orientation parallel to the build direction. The elemental distribution was homogeneous except Mn, which was present in higher concentration in the boundary of melting pool. Chen *et al.*^[14] studied the feasibility of in situ alloying of elemental Mn with pre-alloyed CoCrFeNi in SLM. Only a single FCC phase was found in the resultant materials. The microstructure was characterized to be coarse columnar growing through more than 10 layers in the build direction, and a strong <001> texture was detected. Guo *et al.*^[15] investigated machinability of SLM-produced CoCrFeMnNi. It was found that some machining operations led to compressive stress in machined surface in the cases of milling and grinding, or an increase in tensile stress in the case of wire electrical discharge machining (EDM). Savinov *et al.*^[16] evaluated CoCrFeMnNi HEAs obtained from two major metal AM methods, that is, SLM and laser directed energy deposition (DED) processes. It was shown that both AM methods led to a single-phase FCC material, but the average grain size of DED-produced materials was twice that of SLMed materials.

Tensile properties of CoCrFeMnNi alloy were investigated by Li *et al.*^[13], which showed the increase of ultimate tensile strength with the increase of volumetric energy density until 123 J/mm³, followed by a flattened pattern beyond that. Zhang *et al.*^[17] observed little effect of layer rotation strategy on yield and ultimate tensile strength, which were about 550 and 650 MPa, respectively. Chew *et al.*^[18] studied CoCrFeMnNi manufactured by laser DED. Its tensile strength was found to be higher than the counterpart fabricated by SLM (660 MPa). Besides tensile properties, fracture toughness is also an important material property, which measures how good a given material hinders crack propagation at high-rate loading and is related to the service life and safety of many load-bearing components^[19]. Together with high ductility, toughness is especially important when the SLM-produced HEAs are used as structural materials^[20]. Low toughness

materials generally fail in a brittle manner, which occurs rapidly almost with no plastic deformation^[21], which should be avoided to prevent catastrophic failures. Kim *et al.*^[22] used vacuum induction method (VIM) to fabricate CoCrFeMnNi HEA and showed that its absorbed energy was significantly higher than that of many other alloys. A similar study was performed by Xia *et al.*^[23] who used vacuum levitation melting to produce CoCrFeNi HEA with varying amount of Al addition. It was observed that addition of Al lowered the impact energies at room temperature, and at Al concentrations close to that of Mn in CoCrFeMnNi, toughness dropped from 287.44 J to 1.28 J compared to pure CoCrFeNi. Bi *et al.*^[24] investigated impact toughness of CoCrFeMnNi produced by laser DED. The impact toughness at 0°C was found to be four times smaller compared to the same alloy made by VIM. Kim *et al.*^[25] obtained excellent impact toughness performance at cryogenic temperatures for CoCrFeMnNi produced by SLM, and they attributed the high performance to the formation of many deformation twins.

In general, the as-built alloy components from SLM processes need to receive some form of heat treatment for stress relieving and other purposes. Little information is available regarding heat treatment of additively manufactured CoCrFeMnNi HEA in the literature, and thus, the limited existing research on heat treating CoCrFeMnNi fabricated from other manufacturing processes is summarized in the following. Vaidiya *et al.*^[26] showed that single FCC phases in arc melted CoCrFeNi and CoCrFeMnNi could be retained after thermal exposure at least up to 1373 K for an extended period of time, and the thermal exposure caused no disturbance to elemental distribution. In another study of the same group^[27], a Cr₇C₃ contamination was found whose phase fraction did not change significantly with temperature, suggesting little dissolution of this phase during the thermal exposure up to 1373 K. Laplanche *et al.*^[28] studied inductively melted and casted CoCrFeMnNi that was annealed at 870 – 1270 K for 1 h. Slight increase in hardness was found in materials annealed at lower temperature, which dropped rapidly due to the onset of recrystallization and grain growth. Sathiaraj *et al.*^[29] investigated how heating rate affects microstructure evolution of heavily cold-rolled CoCrFeMnNi HEA. The studied temperature range was between 700°C and 1000°C using high (10°C/s) and low (~0.13°C/s) heating rates. It was found that heating rate significantly affected grain size and grain distribution; low rates led to larger grains with wider size distribution, which is a consequence of early activation of potential nucleation sites.

How a given HEA reacts in a corrosion environment depends on its microstructure, alloying elements, and

processing methods. In recent years, corrosion resistance of CoCrFeMnNi HEA was investigated for samples produced by conventional methods^[30-33], DED^[34] and SLM^[35-38]. Xu *et al.*^[38] compared the corrosion properties of SLMed and as-cast CoCrFeMnNi and found that the former exhibit better corrosion resistance due to homogeneity of components and grain refinements. It was found that the corrosion resistance of HEA thin film in sea water benefits from heat treatment^[33]. However, studies on bulk SLMed HEAs of Al_xCoCrFeMnNi showed that corrosion resistance declines after heat treatment^[35]. Xiang *et al.*^[39] showed that corrosion resistance of SLMed Ti-6Al-4V is dependent upon the laser power and laser scanning speed. However, the trend in relationship between a process parameter and corrosion resistance was not linear, for example, it increased with scan speed up to certain value after which higher scan speeds caused lower corrosion performance while the linear increase of laser power led to oscillating behavior of the resistance.

The critical literature analysis indicates that although CoCrFeMnNi is one of the most studied HEAs, the majority of published works focus on such materials obtained by the conventional processes, such as casting and thin film deposition. For the existing works on CoCrFeMnNi obtained by AM processes, most investigated the as-built materials, but the effects of heat treatment on properties, such as impact fracture and corrosion resistance, remain uncharted. In reality, heat treatment is critical for metal AM in that it provides the stress relief and homogenization for metal alloys after the highly non-equilibrium melting and solidification in the laser AM processes. To bridge the gap, the current work investigates CoCrFeMnNi obtained from the dominant metal AM process, SLM, with a focus on the comparison of microstructure and properties between the as-built and heat-treated materials. It is expected that the findings can shed light on the understanding of CoCrFeMnNi HEA obtained from the complete SLM process, followed by heat treatment.

2. Materials and methods

2.1. SLM experiments

Spherically shaped pre-alloyed particles of equiatomic CoCrFeMnNi, made by gas atomization, were acquired for this study. The particle size distribution ranged from 15 to 53 μm, with an average diameter of 30 μm. A Concept Laser Mlab machine was adopted for SLM fabrication of HEA samples. In the SLM operation, argon was filled in the build chamber to avoid oxidation, and the substrate material is a stainless steel plate. There are two stages of SLM experiments. In the first stage, the appropriate SLM process condition for CoCrFeMnNi on the particular

SLM system was to be obtained. For this purpose, laser power (P), hatch spacing (H), and layer thickness (T) were fixed at 100W, 60 μm , and 20 μm , respectively, while the laser scanning speed (V) was varied from 200 to 800 mm/s. While this study intends to obtain various energy density input by adjusting the scanning speed alone, it is well recognized that other parameters may have significant effect on the obtained properties^[40,41]. Note that the coding of sample conditions combines the numerical value of SLM laser scanning speed and the status of heat treatment. For instance, 450 AB indicates the condition of 450 mm/s. The resultant volume energy density, defined as $P/(V \cdot H \cdot T)$, ranged 104.2 – 416.7 J/mm³. As a result, seven small cubes of 5 × 5.6 × 5 mm were obtained, as shown in Figure 1. Based on the porosity observation and relative density measurement, the appropriate laser scanning speeds were determined for the next stage. In the second stage, with the same settings on laser power, hatch spacing, and layer thickness, two laser scanning speeds were selected for building larger specimens for mechanical property evaluation. Tensile test pieces were produced as a scale-down version of the subsize rectangular tensile test specimen according to ASTM E8/E8M. Their length is 56.4 mm. The length of the specimens was oriented along scan direction (SD), width along the deposit direction (DD), and thickness along transverse direction (TD), as shown in Figure 2. Charpy specimens were prepared in accordance with the ASTM E23 standard, as shown in Figure 3. Each block for Charpy test is 55 mm in length, 10 mm in width, and 10 mm in height.

To investigate the effects of heat treatment (annealing) on the microstructures and mechanical properties, half of the fabricated Charpy samples and half of the tensile samples were heat treated in a vacuum tube furnace (Model: KJ-T1700-60IC). This heat treatment strategy, adopted from other studies^[26,29], consisted of ramping at the rate of 10°C/min up to 1000°C/min, dwell time of 2 h, and then quenching in water.

Electrochemical corrosion experiments were conducted in 3 M NaCl solution at room temperature. Corrosion samples were ground to 1200 grit sandpaper and then polished with 1 μm diamond slurry. Electrochemical studies were performed with a potentiostat (WaveDriver 100)

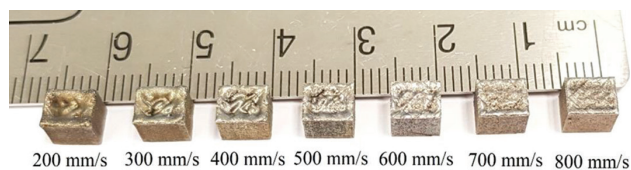


Figure 1. Selective laser melting-produced CoCrFeMnNi test cubes for scanning speed selection.

equipped with a 3-electrode system, which consists of HEA sample working electrode, a Ti wire as a counter electrode, and Ag/AgCl reference electrode. Area of 10 × 10 mm was exposed to the electrolyte. To ensure a steady-state potential, an open circuit potential (OCP) was measured for 1 h. Potentiodynamic polarization curves were performed at a scan rate of 5 mV/s. Five measurements were performed for each condition to ensure the accuracy of the results, which was evaluated by calculating the standard error of these measurements.

2.2. Material characterization

Cubic specimens obtained in the first stage of SLM experiment were analyzed by measuring their density and by visually analyzing their polished side whose normal is perpendicular to DD. Density of these cubes were measured with Archimedes method according to ASTM B962^[42] and compared to the bulk density of 8.05 g/cm³ for CoCrFeMnNi^[36]. Furthermore, the optical micrographs of polished cubic specimens were processed by the software ImageJ, and thus the porosity of obtained materials was obtained. For the specimens obtained in the second stage of SLM experiments, they were cutoff the build plate after SLM using wire EDM. For the Charpy test, V-notch was cut by wire EDM on the surface parallel to DD for the Charpy block specimens. The impact tests were performed using a JBS-300B Charpy Impact Testing Machine. Since the absorbed impact energy of CoCrFeMnNi does not significantly change within a broad temperature range^[22], Charpy test in the current study was performed only at room temperature. Besides the measurement of absorbed impact energy, the lateral expansion on the compression side of the specimens was also evaluated^[43]. For the tensile specimens, tensile tests were performed on a Shimadzu Autograph AGS-X 50 kN machine at a crosshead speed of 1 mm/min at room temperature. Furthermore, Vickers microhardness was obtained on the cross-section (as defined in Figure 2A) of as-built (AB) and heat-treated (HT) samples. The applied load was 0.1 kg with dwell time of 15 s. Nine indentations were made in the matrix array with indentations being 0.5 mm apart from each other.

Metallographic samples were cut, ground, polished and then etched with a solution consisting of C₂H₅OH (25 mL) + HCl (25 mL) + CuSO_{4.5}H₂O (5 g). A scanning electron microscope (model: FEI SCIOS) with electron backscatter diffraction (EBSD) capability was adopted for microstructure and texture analysis. For obtaining reliable results, three EDS area scans at different heights along DD were obtained and the averages were taken. Meanwhile, for phase identification, X-ray diffraction (XRD) profiles were obtained for the materials obtained in the second stage of SLM experiment, using a X'Pert Pro X-ray diffractometer

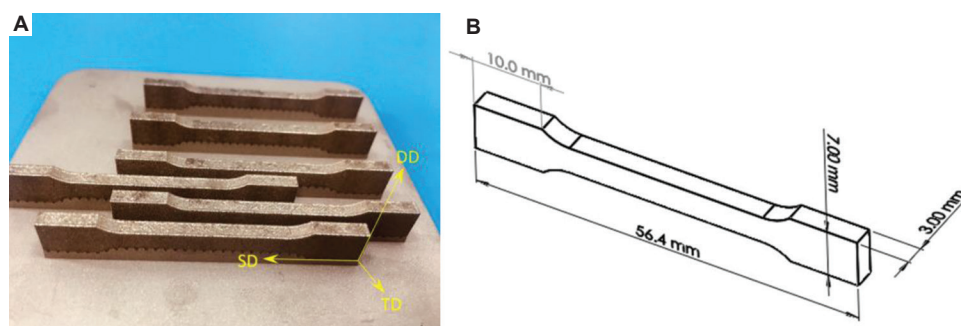


Figure 2. Selective laser melting (SLM)-produced CoCrFeMnNi tensile samples. (A) Selected tensile samples attached to the build plate after SLM; (B) dimensions of tensile samples.

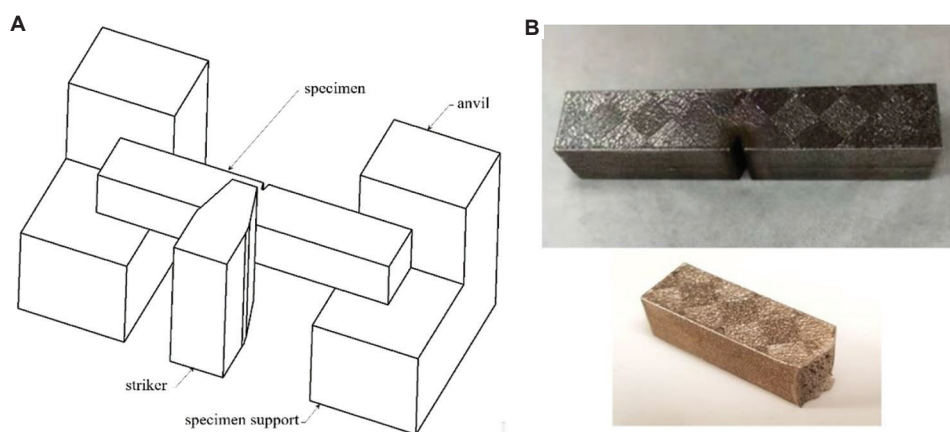


Figure 3. Charpy test of selective laser melting-produced CoCrFeMnNi. (A) Schematic orientation of Charpy specimen during the test (ASTM E23); (B) a Charpy specimen before and after test.

equipped with Cu target. The scan was performed in the 2θ range of 35° to 100° and with tube voltage and current of 40 kV and 44 mA, respectively. The fracture surfaces of Charpy V-notched samples were also characterized by surface appearance as seen in the scanning electron microscopy (SEM) images.

3. Results and discussion

3.1. Effect of scanning speed on relative density and porosity

The criterion for selecting the proper scanning speed was based on the porosity or the density of the SLM-produced materials. Figure 4A shows the optical micrographs of the cross sections of cubic samples obtained under the seven scanning speeds. It is clear that the density and size of pores increase as the scanning speed decreases. This phenomenon can be explained by the following. It is well known that incorrect choices of laser energy density in SLM often result in formation of defects. Depending on defect types, the energy density domain for SLM can be split into three regions. Low energy densities in the first region

usually cause lack of fusion (LOF) defects as laser fails to provide sufficient energy to generate full melting of powder layers, which leads to the formation of pockets of unmelted powder particles or even delamination from the previously deposited layers^[44]. The second region of energy density domain is the target for process parameter optimization and can be characterized by the reduced porosity fraction. In the third region, excessive overheating caused by high energy density generates surface temperatures that exceed the evaporation point of an alloy causing particles and molten material to eject from heat-affected zone, resulting in large spherical pores^[45]. Strong vaporization and spatter lead to shortage of molten metal to fill the molten track. As a result, a printed part is left with many voids^[46]. Moreover, high energy density may cause vaporization of low melting elements, which becomes entrapped and leads to the formation of pores. Inert gas dissolved in the molten metal and released during solidification as well as moisture present on the surface of powder particles may also be the source of gaseous porosity^[45].

In the present study, energy density optimization was performed by varying the scanning speed, and the scope

of chosen values revealed only the latter two regions of energy density domain as explained above. As shown in Figure 4A, laser scanning at slower than 400 mm/s resulted in severe porosity. Notice the top surfaces of the samples are not flat. This is a result of high energy density input used to produce samples in Figure 4. High energy input causes two phenomena that take place in a molten pool. First, the liquid viscosity is too low to keep up the integrity of the melt pool^[47]. Melt pool agitates violently which results in a non-uniform top surface^[48]. Second phenomenon

is a steep thermal gradient that develops due to the high energy input and causes the higher cooling rate. As a result, the molten material does not have enough driving force and time to spread to become flattened. This leads to a big wavy surface at the top of samples^[49]. Figure 4B summarizes the quantitative characterization by means of measured density of cubic samples and visual analysis of percent porosity as observed on their cross section. An overall trend can be observed, that is, higher scanning speeds (within the investigation range) are beneficial for

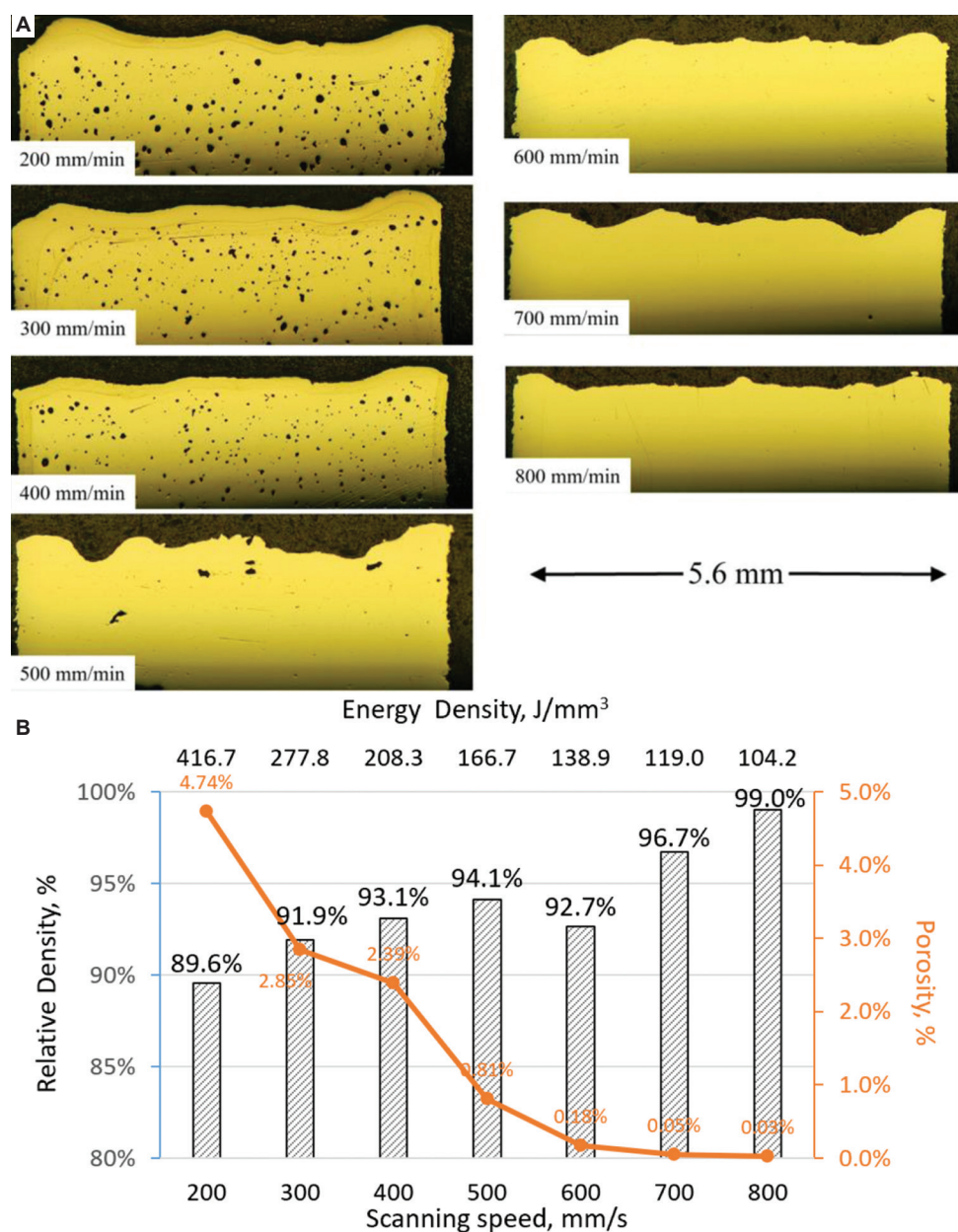


Figure 4. Effect of scanning speed on density and porosity of selective laser melting-produced CoCrFeMnNi. (A) Optical micrographs showing cross sections of printed cubes for process optimization, and (B) density of the cubes measured according to ASTM B962 and porosity measured through image processing.

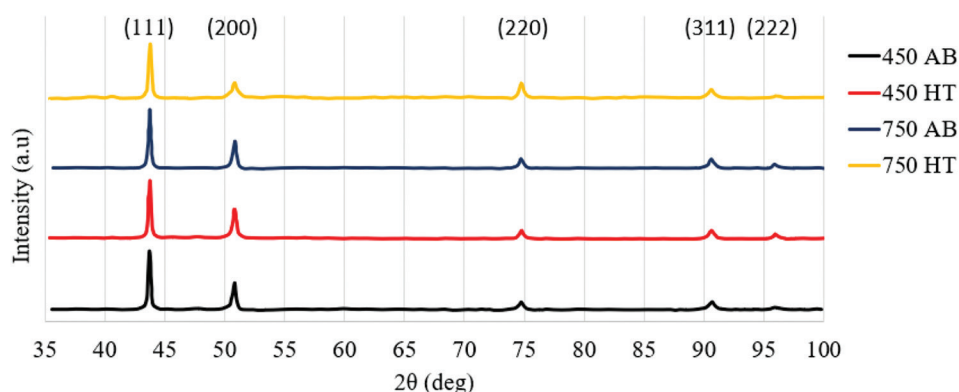


Figure 5. X-ray diffraction analysis results of selective laser melting-produced CoCrFeMnNi at 450 and 750 mm/s scanning speeds before and after heat treatment.

densification of SLM-produced CoCrFeMnNi. It is clear that a scanning speed between 700 and 800 mm/s can lead to very low porosity, and thus the scanning speed of 750 mm/s was chosen to produce samples for mechanical property evaluation. Meanwhile, a scanning speed between 400 and 500 mm/s exhibit acceptable porosity, and thus the scanning speed of 450 mm/s was chosen for comparison purpose. Additional relative density measurements show that the relative density values for 450 mm/s and 750 mm/s are 93.8% and 97.4%, respectively.

3.2. Microstructure analysis

Figure 5 shows the results of XRD analysis for the SLM-produced CoCrFeMnNi using the two scanning speeds of 450 and 750 mm/s before and after heat treatment. FCC single phase was detected in all the four conditions. The XRD results obtained in this study are typical for CoCrFeMnNi produced by laser AM processes, such as SLM^[13,14] and laser DED^[50,51]. No significant shift in peak locations was observed among the studied materials, indicating that the chosen range of scan speed as well as heat treatment had negligible effect on crystal structure and phase composition of the studied materials.

Figure 6 shows SEM images of the DD-TD section of CoCrFeMnNi samples before and after heat treatment. The 450 AB sample consists of layer-wise microstructure, but the melt pool marks are not regularly stacked due to the frequent change of SD. The microstructures of samples before and after heat treatment are very similar, while there is a small difference in average size of melt pools. The average melt pool length of 450 AB condition is about 140 μm , while that 750 AB condition is approximately 120 μm . The smaller size of melt pools of 750 AB sample can be explained by the lower energy density applied in the SLM process. Consequently, less material is melted at the faster scanning speed sample. Heat treatment provides the

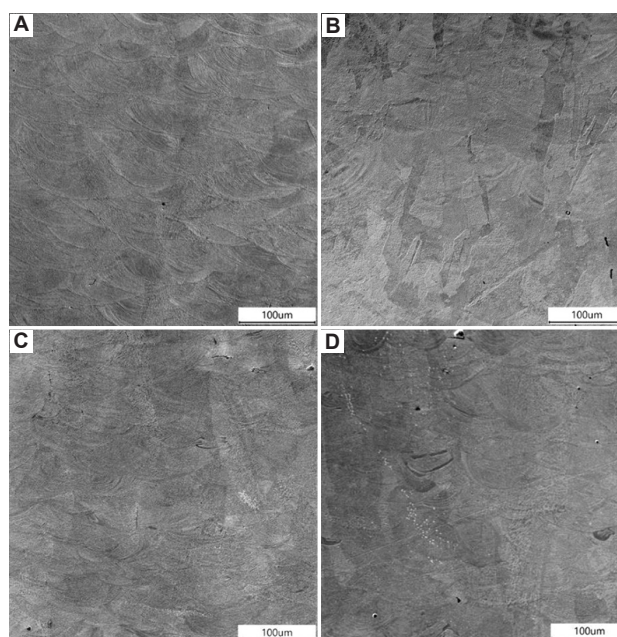


Figure 6. SEM micrographs of selective laser melting-produced CoCrFeMnNi (450 and 750 mm/s scanning speeds, before and after heat treatment) in the DD-TD cross section. (A) 450 AB; (B) 450 HT; (C) 750 AB; and (D) 750 HT.

homogenization effect, and thus the melt pool boundaries are no longer clearly revealed. However, a similar pattern can be observed in terms of elongated grains. The average grain width of 450 HT sample is approximately 85 μm , while that of 750 HT sample is between 50 and 80 μm . Although SEM observations found no such particles, some powder did not fully melt in the SLM process. This is evident from the fact that unmelted particles are present on the fracture surface of Charpy samples (Figure 16E). However, they are not randomly scattered across the fracture surface but only found inside few isolated colonies and therefore should not be present in abundant amount in the obtained materials.

To understand the effect of scan speed and heat treatment on crystallographic texture, EBSD analysis was performed on the DD-TD section. Figure 7 shows the inverse pole figure (IPF) maps as well as PFs for the studied materials. Thanks to the XRD analysis results, only FCC phase was needed to index the pattern for obtaining inverse PFs (IPFs). The confidence index (CI) of all

samples is high (0.62 – 0.65). The microstructure of all four conditions primarily consists of coarse columnar grains of 75 – 200 μm wide, and these grains cross several layers along the deposition direction. Such phenomenon is typical for the morphology for AM-produced materials^[11,20,52,53], which is driven by epitaxial growth due to re-melting in the layer wise process^[54]. The PFs (PFs) show presence of

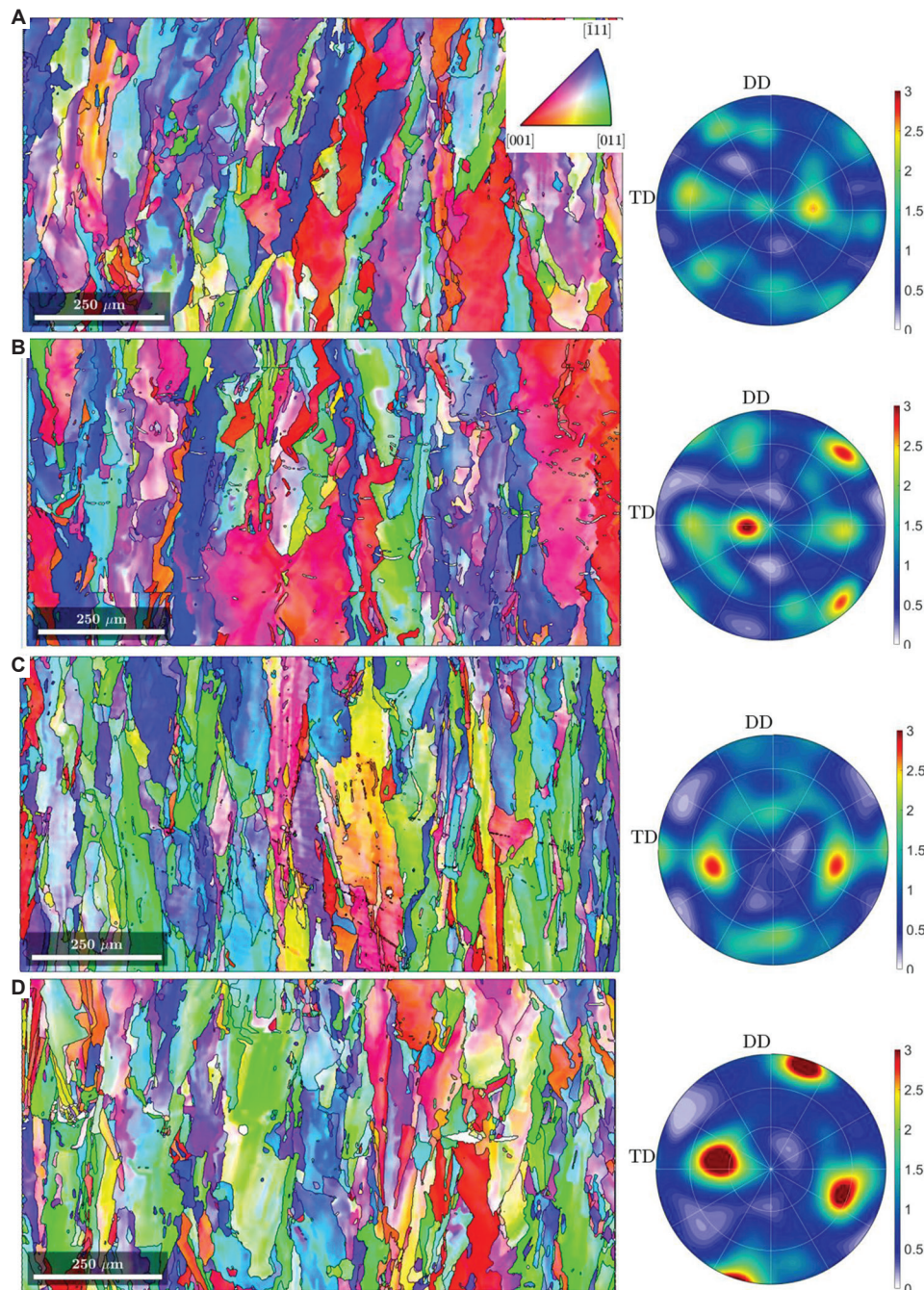


Figure 7. Inverse PFs (IPFs) along the normal direction and their corresponding PFs for SLM-produced CoCrFeMnNi using 450 and 750 mm/s scanning speeds before and after heat treatment. (A) 450 AB; (B) 450 HT; (C) 750 AB; and (D) 750 HT.

texture with a strong <100> alignment in all four samples. However, HT samples appear to have a stronger texture since the intensities of their PFs are higher compared to AB samples, which indicates that heat treatment causes more grains to align with similar orientation. Scanning speed affects the texture as well. The PF intensity of the 750 AB is noticeably higher compared to that of 450 AB. The same is true for heat-treated samples produced with different scanning speeds.

Figure 8 shows grain boundary misorientation distributions for all four conditions. The distribution of all samples is not random and with exception of 450 HT, and all samples feature a single peak with an average misorientation around 45°. Grain boundaries with 45° misorientation mainly correspond to rotation around [100] direction^[55]. Meanwhile, the small angle misorientation (<15°) was reduced after heat treatment for both 450 and 750 mm/s samples. The grain size was calculated using one-dimensional parameter, which refers to the longest distance (diameter) between any two boundary points^[56]. A weighted averaging approach was used to calculate the average grain size using the following equation^[57]:

$$\bar{d}_i = \frac{1}{\sum_{i=0}^n A_i} \sum_{k=0}^n A_i d_i, \quad (I)$$

Where n is the number of grains, A_i is the area of grain I , and d_i is the diameter. As seen from Figure 8, heat

treatment led to increase in average grain size. However, such increase is more pronounced in the 450 mm/s cases for which average grain size increased from 276.5 to 309.3 μm after heat treatment, while in the 750 mm/s cases, grain size increase was more moderate (from 242.1 to 254.4 μm) after heat treatment. Grains of the 450 AB condition are noticeably larger as compared to that of the 750 AB condition for the reasons explained earlier, and similar relationship holds for the HT samples.

As shown in Figure 9, the compositions of both AB and HT samples are overall uniform and close to the equiatomic composition of the original powder. There is a slight misbalance in Cr and Mn with the latter being in a small depletion especially for the 450 mm/s samples. This might be because during the SLM process, the surface temperature of melt pools can exceed the boiling point of the alloy. The difference in vapor pressures on the melt pool surface creates a driving force for vapor to leave the surface^[58]. Mn has the highest vapor pressure and lower melting temperature among other constituents of the HEA and thus can easily leave the melt pool^[59]. Such high volatility of Mn agrees with the current results. Samples of 450 mm/s condition receive higher energy during SLM process leading to higher melt pool temperatures, which hold for longer time. Consequently, higher amount of Mn has a chance to escape resulting in Mn depletion of 450 samples. Heat treatment obviously has no significant effect on Mn content since 1000°C chosen for treatment

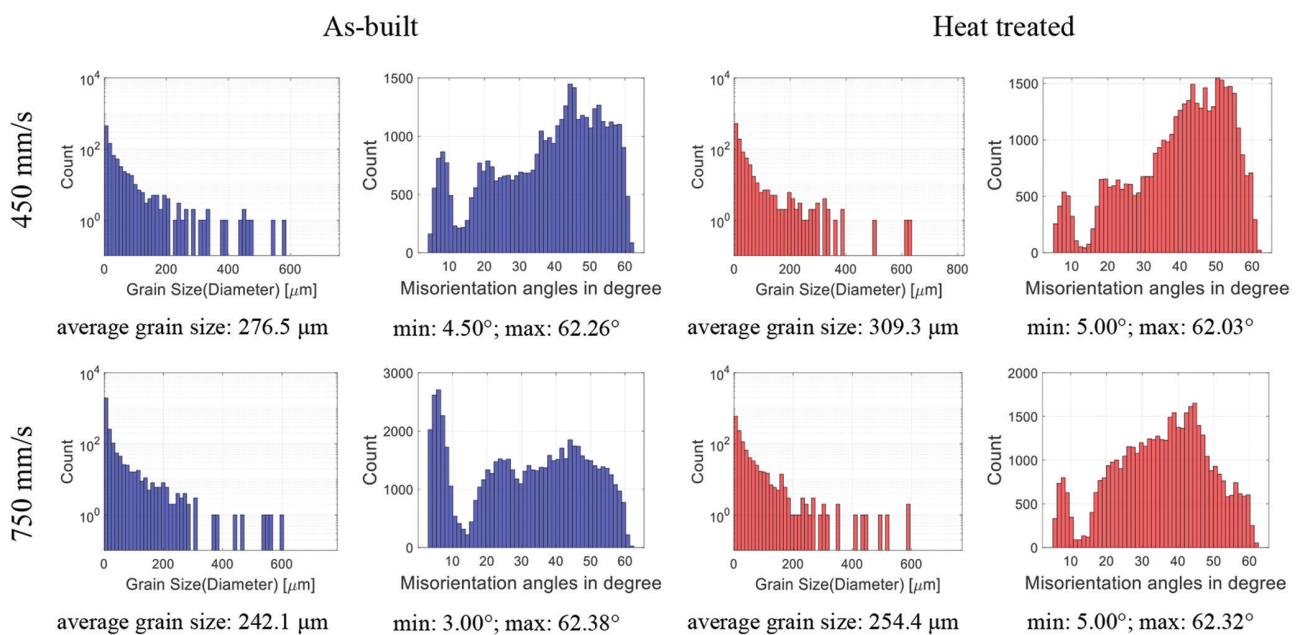


Figure 8. Grain boundaries misorientation distribution and grain area distribution for selective laser melting-produced CoCrFeMnNi using 450 and 750 mm/s scanning speeds before and after heat treatment.

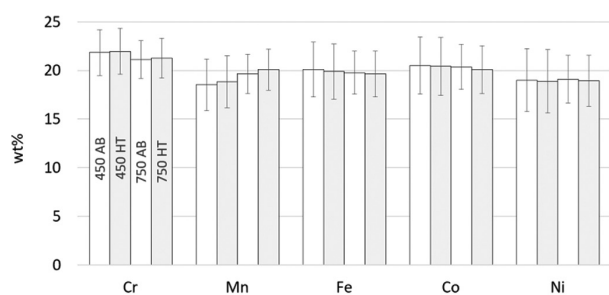


Figure 9. Average composition of selective laser melting-produced CoCrFeMnNi at 450 and 750 mm/s scanning speeds before and after heat treatment.

is far less than the melting temperature of Mn (1246°C). Mn evaporation is believed to contribute to the formation of voids in SLM-produced samples with the higher energy density as discussed above. In the literature, similar phenomenon was observed in SLM-produced CoCrFeMnNi^[36]. Together with the presence of the aforementioned micro-cracks, this slight depletion in Mn might be another indication of the need for further process parameter optimization. On the other hand, the heat treatment hardly affects the composition of SLM-produced CoCrFeMnNi.

3.3. Electrochemical corrosion behavior

Open circuit potential (OCP) is a straightforward method to study the corrosion behavior. Figure 10 shows OCP results for four conditions. Potentials of both AB conditions gradually shift toward the anodic direction or in positive (more noble) potential values. This is an indication that a passive film was formed on the surface of AB samples^[36,60]. The OCP of 750 AB sample has dipped toward the end of the experiment, which is an indication of a breakdown and re-passivation. The opposite phenomenon was observed with OCP of HT samples. OCPs of both 450 HT and 750 HT samples shift towards the cathodic direction or in the negative (less noble) potential values and after 1 h, and the potential stabilizes at about -0.1 V versus normal hydrogen electrode (NHE). In this case, the implication is that passive layers did not form.

Tafel potentiodynamic polarization curves of 450 and 750 samples at AB and HT conditions are shown in Figure 11. Potential at the dip of such curves represents corrosion potential (E_{corr}). This parameter reflects the stability of the system: the higher the E_{corr} and the smaller the corrosion tendency^[37,39]. Figure 12 summarizes the corrosion potentials for all four cases obtained in this experiment. As can be seen from the two figures, higher scanning speed results in slight decrease in corrosion resistance in the AB case. After heat treatment, such

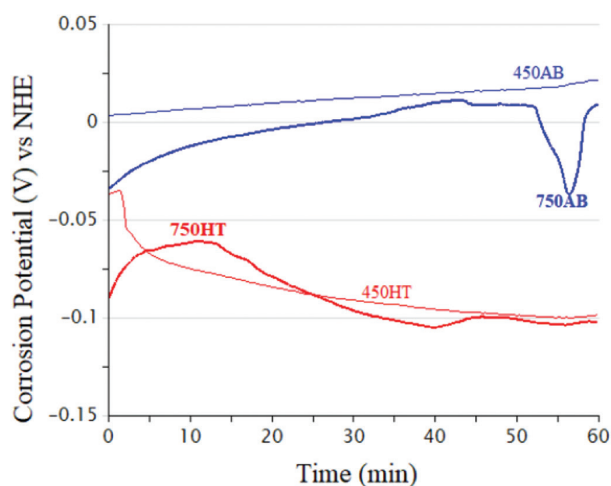


Figure 10. Open circuit potential with respect to normal hydrogen electrode for selective laser melting-produced CoCrFeMnNi at 450 and 750 mm/s scanning speeds, with and without heat treatment.

decrease is more pronounced as E_{corr} of 750 HT case is almost 100 mV <450 HT case. Gradual decrease in corrosion resistance with increase of scan speed was also reported for SLMed Ti-6Al-4V^[39], 316L steel^[61] and CoCrW^[62].

It appears that heat treatment also reduces corrosion resistance of the SLMed CoCrFeMnNi. In some cases, its effect is stronger compared to scan speed. As shown in Figure 12, corrosion potential decreased from -0.200 to -0.216 V versus NHE after heat treatment of 450 sample while it decreases from -0.225 to -0.291 V versus NHE after heat treatment of 750 sample. Corrosion resistance decline was also reported for SLMed AlCoCrMnNi HEA and was attributed to phases formed after heat treatment, which result in less protective passive film^[35]. Zhu *et al.*^[63] reported decrease in corrosion resistance of CoCrFeMnNi with annealing time longer than 6 h. Decrease in the anti-corrosion property was attributed to σ precipitates and Mn-rich inclusions, which increase the susceptibility to pitting corrosion.

3.4. Mechanical properties

3.4.1 Tensile properties

The engineering stress-strain curves, ultimate tensile strength, and elongation of the tensile samples are presented in Figure 13. It can be seen that heat treatment causes only insignificant changes in ultimate tensile strength (<0.5% for the 450 mm/s cases, and up to 4% for the 750 mm/s cases), while it considerably improves the ductility (59.3% and 23.2% increases for the 450 and 750 mm/s cases, respectively). Similar results were observed in spark plasma-sintered CoCrFeMnNi^[3]. Decrease in tensile

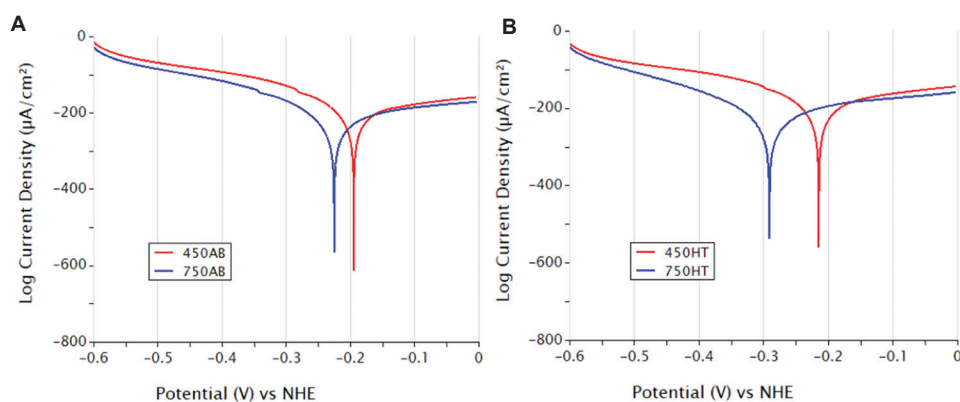


Figure 11. Tafel potentiodynamic polarization curves of selective laser melting-produced CoCrFeMnNi at 450 and 750 mm/s scanning speeds at AB conditions (A) and HT conditions (B).

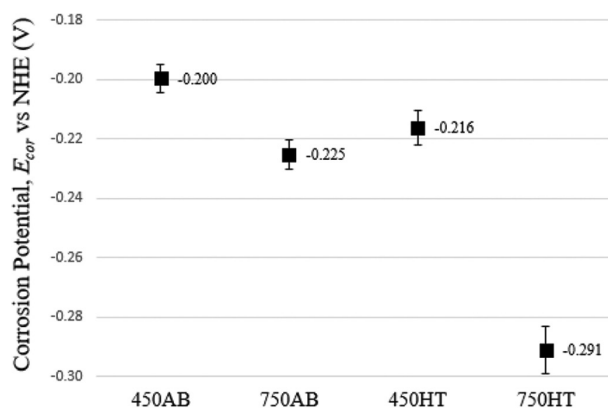


Figure 12. Summary of corrosion potentials for selective laser melting-produced CoCrFeMnNi at 450 and 750 mm/s scanning speeds before and after heat treatment.

strength after heat treatment is usually associated with either the Hall-Petch effect^[13], which establishes the inverse relationship between grain size and tensile strength, or with the formation of precipitates such as carbides along the grain boundaries and plate-like martensitic phases which contribute to stress concentration^[64], or with residual stress caused by lattice distortion^[13]. The more obvious increase in ductility after heat treatment can be attributed to the increase of grain size and reduction of small-angle misorientation (shown in Figure 8), which is a clear indication of release of residual strain induced by SLM process, and restoration of ductility. Note that the obtained tensile properties are in general on par with the reported values from SLM and laser DED processes under the as-built condition. For instance, an ultimate tensile strength value of 601 MPa was achieved for SLM produced CoCrFeMnNi without heat treatment^[65], and an ultimate tensile strength value of 660 MPa was reported for laser DED-produced CoCrFeMnNi without heat treatment^[18].

However, the tensile properties are lower compared with the highest ultimate tensile strength and elongation achieved by the traditional casting process, which were reported to be 763 MPa and 57%, respectively.

3.4.2. Microhardness

Microhardness results for all four conditions, along with the reported values in literature are shown in Figure 14. It appears that the scanning speed does not affect the microhardness of as-built samples. Both 450 AB and 750 AB conditions have practically the same hardness at about 237 HV. In contrast, the microhardness after heat treatment is significantly smaller for both 450 HT and 750 HT conditions. However, the effect of heat treatment on the 750 mm/s sample in terms of microhardness was more pronounced. The hardness of the 750 AB sample decreased by 15% while that of 450 AB sample decreased by only 8.6% after heat treatment. Note that the microhardness values for as-built materials are modestly higher than the hardness of 212 HV1 reported for SLM produced CoCrFeMnNi^[66], and even higher compared to the DED produced CoCrFeMnNi (195 HV5)^[67] and the cast and homogenized (C&H) CoCrFeMnNi (160 HV1)^[68]. In addition, the obtained microhardness values are close to that reported for the same HEA produced by arc melting and drop casting with cold rolling (AMDC&CR) of 21% reduction (222 HV0.3)^[69].

3.4.3. Impact fracture

The Charpy test results are depicted in Figure 15. Similar to the microhardness results, the laser scanning speed has little effect on how much energy has been absorbed by 450 AB and 750 AB conditions. Both have almost the same value of 140 J. However, heat treatment generates noticeable influence on the impact fracture results - the energy absorption for the 450 mm/s samples increased

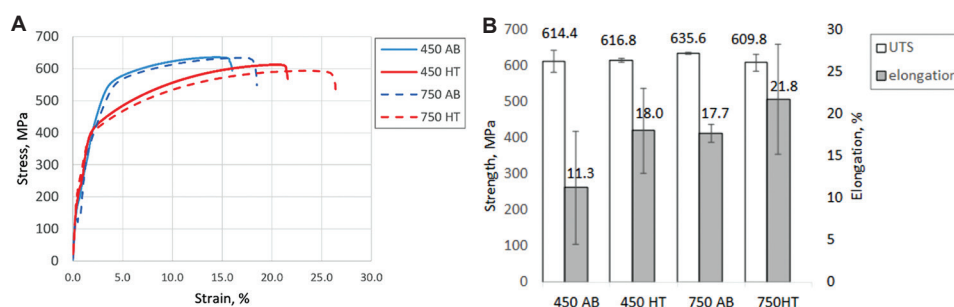


Figure 13. Tensile properties of selective laser melting produced CoCrFeMnNi at 450 and 750 mm/s scanning speeds before and after heat treatment. (A) Room temperature stress-strain curves; (B) ultimate tensile strength and elongation.

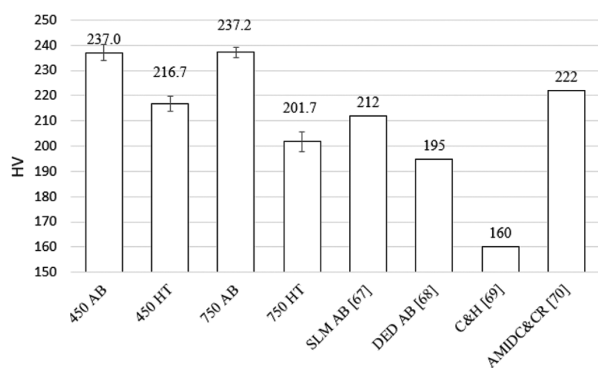


Figure 14. Microhardness results for selective laser melting-produced CoCrFeMnNi at 450 and 750 mm/s scanning speeds before and after heat treatment, along with the microhardness values reported in literature.^[66-69]

by 15.6%, while that for the 750 mm/s samples increased by 11.1%. The absorbed impact energy of both HT and untreated samples are noticeably smaller than the energy absorbed by VIM-produced CoCrFeMnNi (approximately 200 J)^[22] which, in turn, is half that of the forged Al_xCoCrFeNi^[70]. On the other hand, Charpy results of the current study are significantly higher compared to CoCrFeMnNi sample made by DED whose impact energy was measured to be only 50 J at 0°C^[24]. This toughness reduction of SLM-produced samples compared to the cast samples can be attributed to the presence of defects, such as pores, impurities, and brittle, non-equilibrium phases. The latter two were not observed in the present work but the existence of defects, such as LOF and micro-cracks, described above may explain such toughness reduction.

To better understand the impact behavior, fracture surface images of 450 and 750 mm/s samples, both before and after heat treatment, were studied. Higher magnification SEM images reveal features that are characteristic for both ductile and brittle fracture. For instance, Figure 16A shows that vast area of fracture surface is dominant by large dark islands with average size of 50 – 150 μm surrounded by a texture that appears brighter. The observed flat dark islands

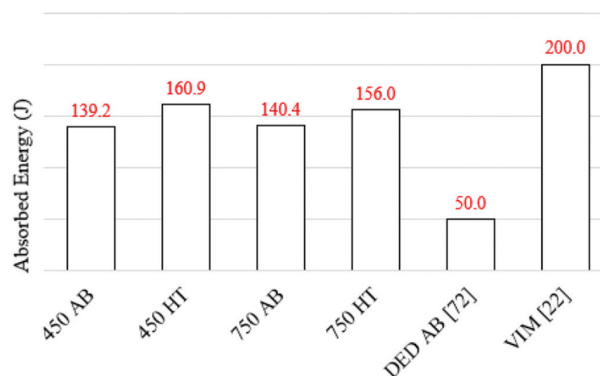


Figure 15. Energy absorption during Charpy test for selective laser melting-produced CoCrFeMnNi at 450 and 750 mm/s scanning speeds before and after heat treatment, along with the reported absorption energies in literature^[22,71]. Note that the DED result^[71] was obtained at 0°C.

are cleavage facets whose presence indicates brittle type fracture^[43,71]. Cleavage facets are surrounded by region that consists of dimples and microvoid coalescence of a submicron size. Abundance of dimple pattern is a typical characteristic of ductile fracture, which is related to the coalescence of microvoids. The microvoids can form due to decohesion between second-phase particle and matrix^[43]. High magnification image in Figure 16B of dimple pattern shows that they were formed by both normal and shear ruptures. When the SEM electron probe hits inclined edge of a dimple, more of secondary electrons escape from it than from the flat surface of cleavage facets. This leads to so-called edge effect leading to brighter appearance of the region that surrounds cleavage facets^[72]. Figure 16C and D shows two cleavage facets whose size differs roughly by an order of magnitude. The smaller one demonstrates clearly defined cleavage steps, river pattern and dimples surrounding the cleavage area, which are similar to the features observed on the fracture surface of AlCoCrCuFeNi HEA^[71]. Besides, unmelted powder particles are observed on fracture surface of all studied samples. In most cases, they are found in a colony of conglomerated particles,

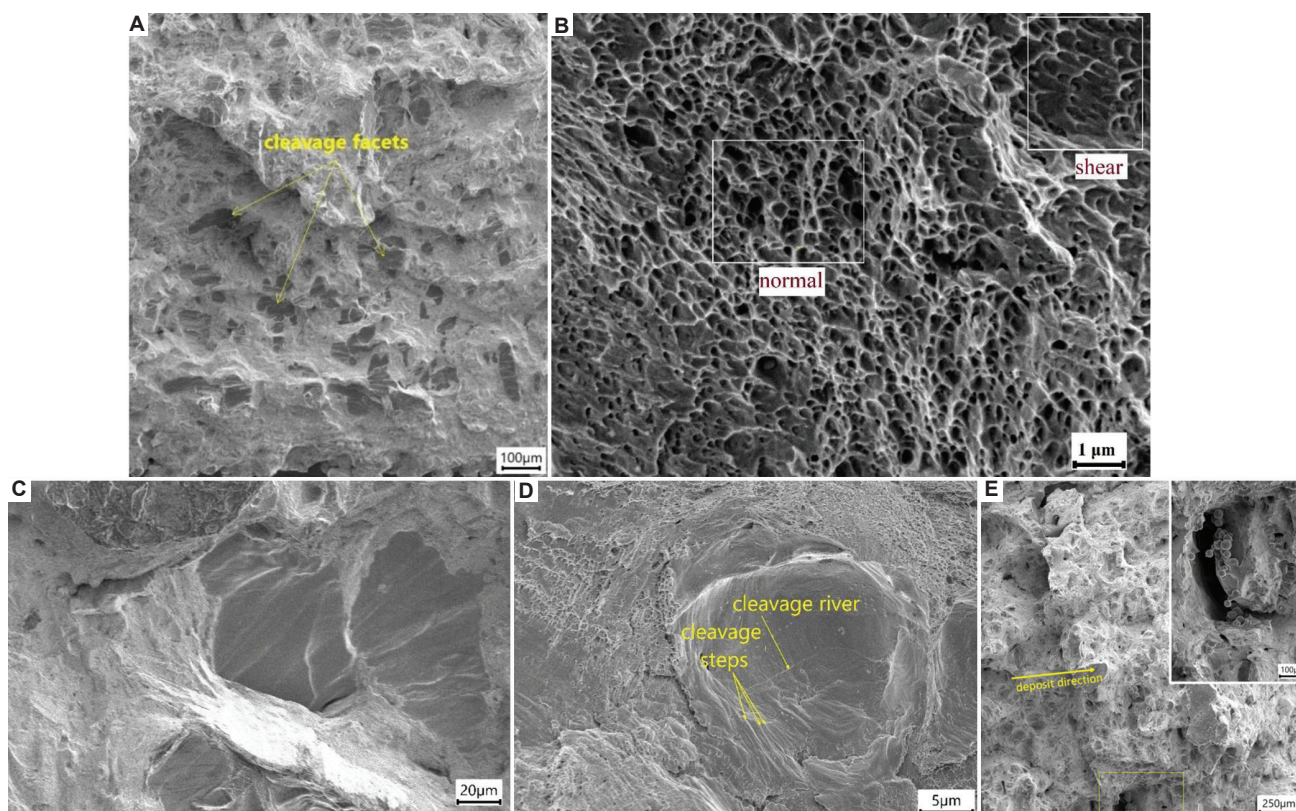


Figure 16. Fracture surface analysis of a 450 AB Charpy sample after testing. (A) Overall observation showing large amount of cleavage facets; (B) a region with dimples formed by normal and shear fractures; (C) a large cleavage facet; (D) a small cleavage facet; (E) colonies of unmelted particles inside a void.

inside either large voids or wide cracks, as shown in [Figure 16E](#). These colonies of unmelted powder particles are surrounded by a smooth surface without cleavage steps or river pattern suggesting that the cause of fracture in the vicinity of unmelted powder particles is LOF.

[Figure 17](#) shows low magnification image of surface of the 450 and 750 samples before and after heat treatment. There is a clear difference between the fracture surface morphology before and after heat treatment. The amount and size of cleavage facets of the HT sample are smaller compared to the AB sample while more ductile dimples can be observed on the surface of the HT sample. Both materials have lots of slightly curved deep cracks with their concave up direction pointing toward the deposit direction. Their positions are generally aligned with a straight line orthogonal to the deposition direction (marked as dashed line), which suggests that they are situated on the same deposited layer. In addition, almost all such cracks are free of unmelted powder particles. The fact that these cracks are found in HT samples as well suggests that the chosen heat treatment is not effective for the reduction of these defects, and perhaps hot isostatic pressing (HIP) treatment

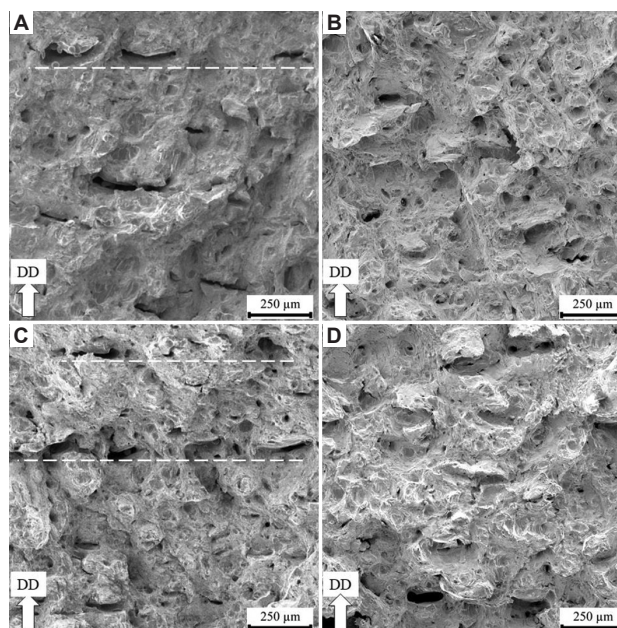


Figure 17. Fracture surface of (A) 450 AB, (B) 450 HT, (C) 750 AB, and (D) 750 HT Charpy samples showing wide cracks originated on lack of fusion defects.

can help to eliminate or reduce the amount of such defects and therefore significantly increase impact toughness of SLM-produced CoCrFeMnNi.

4. Conclusions

This research focuses on the effect of heat treatment on microstructure and properties of SLM-produced CoCrFeMnNi, in which the impact fracture and corrosion resistance were, for the first time, studied. First, SLM experiments were performed with various laser scanning speeds, and the proper ones were determined based on the evaluation on the density and porosity of obtained CoCrFeMnNi. In the next step, various samples such as Charpy impact and tensile test were prepared with the selected SLM process parameters, and heat treatment was conducted on the obtained materials. Thereafter, corrosion resistance properties, tensile properties, impact fracture, microhardness, elemental composition, and crystallographic texture were investigated for the as-built and heat treated samples. The following findings can be summarized.

- Under the fixed settings of the laser power (P), hatch spacing (H), and layer thickness (T) at 100W, 60 μm , and 20 μm , respectively, the laser scanning speed between 700 and 800 mm/s was found to generate the highest density and lowest porosity.
- SLM-produced CoCrFeMnNi materials solidified into a single-phase FCC structure. While the texture with a strong $\langle 100 \rangle$ alignment was observed in the materials obtained using 450 mm/s and 650 mm/s scanning speeds, for both before and after heat treatment, the texture of heat-treated materials was found to be stronger according to the PFs.
- Elemental composition of obtained samples is close to the nominal composition of equiatomic CoCrFeMnNi. However, small depletion of Mn was detected especially in 450 mm/s cases, which can be attributed to the high volatility of Mn in the SLM process.
- Ductility was drastically improved by the heat treatment (increased by 59.3% and 23.2% for 450 mm/s and 750 mm/s cases, respectively), while the ultimate tensile strength showed only negligible change. It could be attributed to the release of residual strain and the increase of average grain size as a result of heat treatment.
- Between the selected 450 mm/s and 750 mm/s scanning speeds, the difference in impact energy absorption was small. However, heat treatment caused noticeable increase in energy absorption (by 15.6% and 11.1% for 450 mm/s and 750 mm/s cases, respectively).

- Electrochemical corrosion study revealed formation of passive film on surface of both AB samples as evident from anodic drift of open circuit potential test while no such films were formed on heat-treated samples. Higher scanning speed resulted in slight decrease in corrosion resistance in the as-built materials. Heat treatment also lowered the corrosion resistance, which is more pronounced for the materials obtained at 750 mm/s.

Acknowledgments

None.

Funding

None.

Conflict of interest

The authors hereby declare that they have no known competing financial interests or personal relationships that could have appeared to influence the work reported in this paper.

Author contributions

Conceptualization: Jing Shi

Data curation: Roman Savinov

Formal analysis: Roman Savinov

Investigation: Roman Savinov

Methodology: Roman Savinov

Supervision: Jing Shi

Visualization: Roman Savinov, Jing Shi

Writing – original draft: Roman Savinov, Jing Shi

Writing – reviewing and editing: Roman Savinov, Jing Shi

Availability of data

The raw/processed data required to reproduce the findings can be made available on reasonable requests.

References

1. Moghaddam AO, Shaburova NA, Samodurova MN, *et al.*, 2021, Additive manufacturing of high entropy alloys: A practical review. *J Mater Sci Technol*, 77: 131–162.
2. Yeh JW, Chen SK, Lin SJ, *et al.*, 2004, Nanostructured high-entropy alloys with multiple principal elements: novel alloy design concepts and outcomes. *Adv Eng Mater*, 6: 299–303.
3. Eißmann N, Klöden B, Weißgärber T, *et al.*, 2017, High-entropy alloy CoCrFeMnNi produced by powder metallurgy. *Powder Metallurgy*, 60: 184–197.
4. Wang X, Guo W, Fu Y, 2021, High-entropy alloys: Emerging materials for advanced functional applications. *J Mater Chem A*, 9: 663–701.

5. Chen S, Tong Y, Liaw PK, 2018, Additive manufacturing of high-entropy alloys: A review. *Entropy*, 20: 937. <https://doi.org/10.3390/e20120937>
6. Cantor B, Chang ITH, Knight P, *et al.*, 2004, Microstructural development in equiatomic multicomponent alloys. *Mater Sci Eng A*, 375: 213–218.
7. Zaddach AJ, Niu C, Koch CC, *et al.*, 2013, Mechanical properties and stacking fault energies of NiFeCrCoMn high-entropy alloy. *JOM*, 65: 1780–1789.
8. Drissi-Daoudi R, Pandiyan V, Logé R, *et al.*, 2022, Differentiation of materials and laser powder bed fusion processing regimes from airborne acoustic emission combined with machine learning. *Virtual Phys Prototyp*, 17: 181–204.
9. Sing SL, 2022, Perspectives on additive manufacturing enabled Beta-titanium alloys for biomedical applications. *Int J Bioprint*, 8: 478. <https://doi.org/10.18063/ijb.v8i1.478>
10. Shi J, Wang Y, 2020, Development of metal matrix composites by laser-assisted additive manufacturing technologies: A review. *J Mater Sci*, 55: 9883–9917.
11. Wang Y, Shi J, Liu Y, 2019, Competitive grain growth and dendrite morphology evolution in selective laser melting of Inconel 718 superalloy. *J Cryst Growth*, 521: 15–29.
12. Brif Y, Thomas M, Todd I, 2015, The use of high-entropy alloys in additive manufacturing. *Scr Mater*, 99: 93–96.
13. Li R, Niu P, Yuan T, *et al.*, 2018, Selective laser melting of an equiatomic CoCrFeMnNi high-entropy alloy: Processability, non-equilibrium microstructure and mechanical property. *J Alloys Compounds*, 746: 125–134.
14. Chen P, Li S, Zhou Y, *et al.*, 2020, Fabricating CoCrFeMnNi high entropy alloy via selective laser melting *in-situ* alloying. *J Mater Sci Technol*, 43: 40–43.
15. Guo J, Goh M, Zhu Z, *et al.*, 2018, On the machining of selective laser melting CoCrFeMnNi high-entropy alloy. *Mater Des*, 153: 211–220.
16. Savinov R, Wang Y, Wang J, *et al.*, 2021, Comparison of microstructure and properties of CoCrFeMnNi high-entropy alloy from selective laser melting and directed energy deposition processes. *Procedia Manuf*, 53: 435–442.
17. Zhang C, Feng K, Kokawa H, *et al.*, 2020, Cracking mechanism and mechanical properties of selective laser melted CoCrFeMnNi high entropy alloy using different scanning strategies. *Mater Sci Eng A*, 789: 139672.
18. Chew Y, Bi GJ, Zhu ZG, *et al.*, 2019, Microstructure and enhanced strength of laser aided additive manufactured CoCrFeNiMn high entropy alloy. *Mater Sci Eng A*, 744: 137–144.
19. Keshavarz MK, Sikan F, Boutet CE, *et al.*, 2019, Impact properties of half stress-relieved and hot isostatic pressed Ti–6Al–4V components fabricated by laser powder bed fusion. *Mater Sci Eng A*, 760: 481–488.
20. Lee KA, Kim YK, Yu JH, *et al.*, 2017, Effect of heat treatment on microstructure and impact toughness of Ti–6Al–4V manufactured by selective laser melting process. *Arch Metallurgy Mater*, 62: 1341–1346.
21. Krishnadev M, Larouche M, Lakshmanan VI, *et al.*, 2010, Failure analysis of failed wire rope. *J Failure Anal Prev*, 10: 341–348.
22. Kim JH, Lim KR, Won JW, *et al.*, 2018, Mechanical properties and deformation twinning behavior of as-cast CoCrFeMnNi high-entropy alloy at low and high temperatures. *Mater Sci Eng A*, 712: 108–113.
23. Xia SQ, Gao MC, Zhang Y, 2018, Abnormal temperature dependence of impact toughness in AlxCoCrFeNi system high entropy alloys. *Mater Chem Phys*, 210: 213–221.
24. Bi G, Chew Y, Weng F, *et al.*, 2018, Process study and characterization of properties of FeCrNiMnCo high-entropy alloys fabricated by laser-aided additive manufacturing. In: *Advanced Laser Processing and Manufacturing II*. Vol. 10813. United States: SPIE. pp. 43–52.
25. Kim YK, Kim MC, Lee KA, 2022, 1.45 GPa ultrastrong cryogenic strength with superior impact toughness in the *in-situ* nano oxide reinforced CrMnFeCoNi high-entropy alloy matrix nanocomposite manufactured by laser powder bed fusion. *J Mater Sci Technol*, 97: 10–19.
26. Vaidya M, Guruvidyathri K, Murty BS, 2019, Phase formation and thermal stability of CoCrFeNi and CoCrFeMnNi equiatomic high entropy alloys. *J Alloys Compounds*, 774: 856–864.
27. Vaidya M, Anupam A, Bharadwaj JV, *et al.*, 2019, Grain growth kinetics in CoCrFeNi and CoCrFeMnNi high entropy alloys processed by spark plasma sintering. *J Alloys Compounds*, 791: 1114–1121.
28. Laplanche G, Horst O, Otto F, *et al.*, 2015, Microstructural evolution of a CoCrFeMnNi high-entropy alloy after swaging and annealing. *J Alloys Compounds*, 647: 548–557.
29. Sathiaraj GD, Tsai CW, Yeh JW, *et al.*, 2016, The effect of heating rate on microstructure and texture formation during annealing of heavily cold-rolled equiatomic CoCrFeMnNi high entropy alloy. *J Alloys Compounds*, 688: 752–761.
30. Aiso T, Nishimoto M, Muto I, *et al.*, 2021, Roles of alloying elements in the corrosion resistance of equiatomic CoCrFeMnNi high-entropy alloy and application to corrosion-resistant alloy design. *Mater Trans*, 62: 1677–1680.
31. Pathak S, Kumar N, Mishra RS, *et al.*, 2019, Aqueous corrosion behavior of cast CoCrFeMnNi alloy. *J Mater Eng Perform*, 28: 5970–5977.
32. Peng H, Lin Z, Li R, *et al.*, 2020, Corrosion behavior of an equiatomic CoCrFeMnNi high-entropy alloy—a comparison between selective laser melting and cast. *Front Mater*, 7: 244.
33. Popescu AMJ, Branzoi F, Burada M, *et al.*, 2022, Influence of

- heat treatment on the corrosion behavior of electrodeposited CoCrFeMnNi high-entropy alloy thin films. *Coatings*, 12; 1108.
<https://doi.org/10.3390/coatings12081108>
34. Melia MA, Carroll JD, Whetten SR, *et al.*, 2019, Mechanical and corrosion properties of additively manufactured CoCrFeMnNi high entropy alloy. *Addit Manuf*, 29: 100833.
 35. Kong D, Wang L, Zhu G, *et al.*, 2023, Heat treatment effects on the metastable microstructure, mechanical property and corrosion behavior of Al-added CoCrFeMnNi alloys fabricated by laser powder bed fusion. *J Mater Sci Technol*, 138: 171–182.
 36. Ren J, Mahajan C, Liu L, *et al.*, 2019, Corrosion behavior of selectively laser melted CoCrFeMnNi high entropy alloy. *Metals*, 9: 1029.
 37. Wang B, Sun M, Li B, *et al.*, 2020, Anisotropic response of CoCrFeMnNi high-entropy alloy fabricated by selective laser melting. *Materials*, 13: 5687.
<https://doi.org/10.3390/ma13245687>
 38. Xu Z, Zhang H, Du X, *et al.*, 2020, Corrosion resistance enhancement of CoCrFeMnNi high-entropy alloy fabricated by additive manufacturing. *Corrosion Sci*, 177: 108954.
 39. Xiang S, Yuan Y, Zhang C, *et al.*, 2022, Effects of process parameters on the corrosion resistance and biocompatibility of Ti6Al4V parts fabricated by selective laser melting. *ACS Omega*, 7: 5954–5961.
 40. Cacace S, Semeraro Q, 2022, Fast optimisation procedure for the selection of L-PBF parameters based on utility function. *Virtual Phys Prototyp*, 17: 125–137.
 41. Gong X, Zeng D, Groeneveld-Meijer W, *et al.*, 2022, Additive manufacturing: A machine learning model of process-structure-property linkages for machining behavior of Ti-6Al-4V. *Mater Sci Addit Manuf*, 1: 6.
 42. Lu C, Shi J, 2022, Relative density and surface roughness prediction for Inconel 718 by selective laser melting: Central composite design and multi-objective optimization. *Int J Adv Manuf Technol*, 119: 3931–3949.
 43. Davis JR, 1998, *Metals Handbook*. Handbook Committee. Netherlands: ASM International.
 44. Maitra V, Shi J, Lu C, 2022, Robust prediction and validation of as-built density of Ti-6Al-4V parts manufactured via selective laser melting using a machine learning approach. *J Manuf Processes*, 78: 183–201.
 45. Cherry JA, Davies HM, Mehmood S, *et al.*, 2015, Investigation into the effect of process parameters on microstructural and physical properties of 316L stainless steel parts by selective laser melting. *Int J Adv Manuf Technol*, 76: 869–879.
 46. Bai Y, Yang Y, Wang D, *et al.*, 2017, Influence mechanism of parameters process and mechanical properties evolution mechanism of maraging steel 300 by selective laser melting. *Mater Sci Eng A*, 703: 116–123.
 47. Ye D, Zhu K, Fuh JY, *et al.*, 2019, The investigation of plume and spatter signatures on melted states in selective laser melting. *Optics Laser Technol*, 111: 395–406.
 48. Dai S, Zhu H, Zeng X, 2020, Effect of line energy density and wall thickness on the top surface quality of AlSi10Mg sample fabricated via selective laser melting. In: *IOP Conf Ser Mater Sci Eng*, 774: 012088.
 49. Pal S, Lojen G, Hudak R, *et al.*, 2020, As-fabricated surface morphologies of Ti-6Al-4V samples fabricated by different laser processing parameters in selective laser melting. *Addit Manuf*, 33: 101147.
 50. Xiang S, Luan H, Wu J, *et al.*, 2019, Microstructures and mechanical properties of CrMnFeCoNi high entropy alloys fabricated using laser metal deposition technique. *J Alloys Compounds*, 773: 387–392.
 51. Wang Q, Amar A, Jiang C, *et al.*, 2020, CoCrFeNiMo0.2 high entropy alloy by laser melting deposition: Prospective material for low temperature and corrosion resistant applications. *Intermetallics*, 119: 106727.
 52. Bian P, Shi J, Liu Y, *et al.*, 2020, Influence of laser power and scanning strategy on residual stress distribution in additively manufactured 316L steel. *Optics Laser Technol*, 132: 106477.
 53. Joseph J, Stanford N, Hodgson P, *et al.*, 2017, Tension/compression asymmetry in additive manufactured face centered cubic high entropy alloy. *Scripta Mater*, 129: 30–34.
 54. Wang Y, Shi J, Lu S, *et al.*, 2017, Selective laser melting of graphene-reinforced Inconel 718 superalloy: evaluation of microstructure and tensile performance. *J Manuf Sci Eng*, 139: 041005.
 55. Ratanaphan S, Yoon Y, Rohrer GS, 2014, The five parameter grain boundary character distribution of polycrystalline silicon. *J Mater Sci*, 49: 4938–4945.
 56. Bachmann F, Hielscher R, Schaeben H, 2010, Texture analysis with MTEX—free and open source software toolbox. In: *Solid State Phenomena*. Vol. 160. Switzerland: Trans Tech Publications Ltd. pp. 63–68.
 57. Wright S, 2014, Time for a Change—New Perspectives in Grain Size Analysis. Available from: <https://www.edaxblog.com/2014/06/23/time-for-a-change-new-perspectives-in-grain-size-analysis> [Last accessed on 2023 Jan 10].
 58. He X, DebRoy T, Fuerschbach PW, 2003, Alloying element vaporization during laser spot welding of stainless steel. *J Phys D Appl Phys*, 36: 3079.
 59. Alcock CB, Itkin VP, Horrigan MK, 1984, Vapour pressure equations for the metallic elements: 298–2500K. *Can Metallurgical Q*, 23: 309–313.
 60. Mouanga M, Berçot P, 2010, Comparison of corrosion behaviour of zinc in NaCl and in NaOH solutions; Part II: Electrochemical analyses. *Corrosion Sci*, 52: 3993–4000.
 61. Collazo A, Figueroa R, Pérez C, *et al.*, 2022, Effect of laser speed and hatch spacing on the corrosion behavior of 316L stainless steel produced by selective laser melting. *Materials*,

- 15: 1353.
62. Lu Y, Gan Y, Lin J, *et al.*, 2017, Effect of laser speeds on the mechanical property and corrosion resistance of CoCrW alloy fabricated by SLM. *Rapid Prototyp J*, 23: 28–33.
 63. Zhu M, Zhao B, Yuan Y, *et al.*, 2021, Effect of annealing time on microstructure and corrosion behavior of CoCrFeMnNi high-entropy alloy in alkaline soil simulation solution. *Corrosion Commun*, 3: 45–61.
 64. Sing SL, Huang S, Yeong WY, 2020, Effect of solution heat treatment on microstructure and mechanical properties of laser powder bed fusion produced cobalt-28chromium-6molybdenum. *Mater Sci Eng A*, 769: 138511.
 65. Gludovatz B, Hohenwarter A, Catoor D, *et al.*, 2014, A fracture-resistant high-entropy alloy for cryogenic applications. *Science*, 345: 1153–1158.
 66. Piglione A, Dovggy B, Liu C, *et al.*, 2018, Printability and microstructure of the CoCrFeMnNi high-entropy alloy fabricated by laser powder bed fusion. *Mater Lett*, 224: 22–25.
 67. Haase C, Tang F, Wilms MB, *et al.*, 2017, Combining thermodynamic modeling and 3D printing of elemental powder blends for high-throughput investigation of high-entropy alloys—Towards rapid alloy screening and design. *Mater Sci Eng A*, 688: 180–189.
 68. Schuh B, Mendez-Martin F, Völker B, *et al.*, 2015, Mechanical properties, microstructure and thermal stability of a nanocrystalline CoCrFeMnNi high-entropy alloy after severe plastic deformation. *Acta Mater*, 96: 258–268.
 69. Otto F, Hanold NL, George EP, 2014, Microstructural evolution after thermomechanical processing in an equiatomic, single-phase CoCrFeMnNi high-entropy alloy with special focus on twin boundaries. *Intermetallics*, 54: 39–48.
 70. Li D, Zhang Y, 2016, The ultrahigh charpy impact toughness of forged AlxCoCrFeNi high entropy alloys at room and cryogenic temperatures. *Intermetallics*, 70: 24–28.
 71. Zhang Y, Zuo TT, Tang Z, *et al.*, 2014, Microstructures and properties of high-entropy alloys. *Progress Mater Sci*, 61: 1–93.
 72. Leng Y, 2009, *Materials characterization: Introduction to Microscopic and Spectroscopic Methods*. United States: John Wiley & Sons.